

Absence of Oxygen-Vacancy-Related Deep Levels in the Amorphous Mixed Oxide $(\text{Al}_2\text{O}_3)_{1-x}(\text{SiO}_2)_x$: First-Principles Exploration of Gate Oxides in GaN-Based Power Devices

Kenta Chokawa^{1,*}, Tetsuo Narita², Daigo Kikuta², Koji Shiozaki², Tetsu Kachi², Atsushi Oshiyama¹, and Kenji Shiraishi¹

¹ Institute of Materials and Systems for Sustainability, Nagoya University, Furo-cho, Chikusa-ku, Nagoya 464-8601, Japan

² Toyota Central R&D Labs., Inc., Nagakute, Aichi 480-1192, Japan

(Received 9 July 2019; revised 30 April 2020; accepted 21 May 2020; published 13 July 2020)

We report density-functional calculations that clarify the atomic and electronic structures of the oxygen vacancy V_O in amorphous $(\text{Al}_2\text{O}_3)_{1-x}(\text{SiO}_2)_x$ mixed oxides, which are promising candidates for the gate insulator in GaN technology. We construct microscopic models of the amorphous structure by the melt-quench scheme and then examine all the possible oxygen vacancies and determine the total-energy-minimized V_O structures. We find a clear tendency for V_O 's formed at oxygen sites surrounded by fewer Al atoms to have a lower formation energy. More importantly, we find that a V_O surrounded by Si atoms alone does not induce deep levels in the energy gap of GaN, whereas V_O 's surrounded by some Al atoms induce a deep level. This theoretical finding strongly implies that the majority of V_O 's in amorphous $(\text{Al}_2\text{O}_3)_{1-x}(\text{SiO}_2)_x$ are electrically inactive and not very harmful to device operation. Further, we explore the possibilities for structural transformation from the electrically active V_O to the electrically inactive V_O . We identify reaction pathways for such transformations and obtain the corresponding energy barriers. The calculated occurrence rate for these transformations is high enough to ensure that thermal annealing at typical temperatures and times causes conversion of electrically active V_O 's to inactive V_O 's, providing a further advantage of $(\text{Al}_2\text{O}_3)_{1-x}(\text{SiO}_2)_x$ as a gate insulator over other oxides such as SiO_2 and Al_2O_3 .

DOI: 10.1103/PhysRevApplied.14.014034

I. INTRODUCTION

The development of power electronics, exemplified by high-performance electron devices such as metal-oxide-semiconductor field-effect transistors (MOSFETs), insulated-gate bipolar transistors, and high-electron-mobility transistors, is imperative to advancing energy saving in our society. Among these device structures, the MOSFET has an advantage due to the controllability of its threshold voltage, leading to reliable device operation in harsh environments. However, this advantage is guaranteed only by the existence of high-quality gate-insulator films that can shut off the leakage current. Exploration of insulating films with a leakage current as small as possible is therefore essential in the design of MOSFETs. There are three important characteristics of a gate insulator that facilitate a small leakage current in MOSFETs: a high dielectric constant of the insulator, a large offset in the band alignment at the insulator-semiconductor interface, and a low defect density in the insulator and at the interface.

Currently, the main material that power devices are composed of is silicon. This is due to the presence of high-quality insulating SiO_2 films, which are easily formed by thermal oxidation of the Si surface. It is said that if SiO_2 had not existed, Si-related technology would not have even started. Silicon carbide (SiC), which has advantages from a materials viewpoint such as a wider band gap and robustness in harsh environments compared with Si, is emerging as a replacement for Si [1–4]. For insulating films in devices, SiO_2 formed by oxidation or deposition is again used [5,6], and SiC MOSFETs are already on the market [4,7]. The superiority of SiO_2 arises from its large offset with respect to the conduction and valence bands of the semiconductors used for channels.

GaN, which is commonly used in optoelectronics [8–10], is also a promising material for power electronics: its wide band gap and robustness, similar to those of SiC, and its higher mobility than that of SiC promise usefulness in power electronics [11–14]. However, a serious disadvantage of GaN as a material for power MOSFETs is, at present, the lack of good gate-insulator films.

Thermal oxidation of GaN usually produces Ga_2O_3 insulating films. This insulator, however, is unsuitable for

*chokawa@nagoya-u.jp

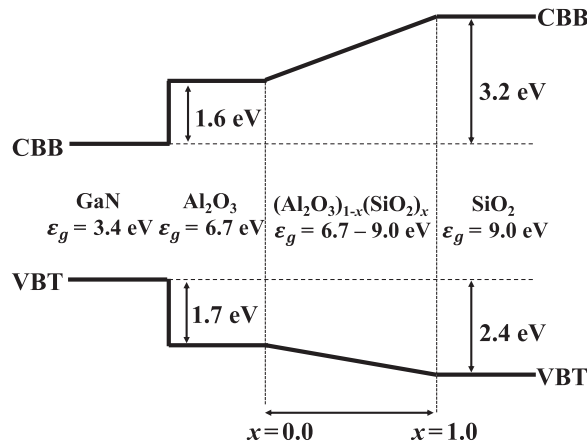


FIG. 1. Schematic band alignment at an interface between GaN and amorphous $(\text{Al}_2\text{O}_3)_{1-x}(\text{SiO}_2)_x$ mixed oxide deduced from photoemission spectroscopy [24]. The conduction-band bottom (CBB) and valence-band top (VBT) of GaN (leftmost), Al_2O_3 (next left), SiO_2 (rightmost), and $(\text{Al}_2\text{O}_3)_{1-x}(\text{SiO}_2)_x$ are shown by thick solid lines.

gate dielectrics in GaN technology: the conduction-band offset (CBO) of the Ga_2O_3 with respect to the GaN is too small to ensure device operation [15]. Hence, deposition of SiO_2 or Al_2O_3 , both of which show a large CBO and valence-band offset (VBO) with respect to GaN, has become a promising fabrication technique for forming GaN-based MOS devices [16–23]. It is expected that the gate leakage current can be suppressed with SiO_2 films due to the large band gap of SiO_2 (9.0 eV) and CBO (3.2 eV), as shown in Fig. 1 [24]. However, SiO_2 has the disadvantage of a relatively small dielectric constant ($\epsilon = 3.8$), which requires thicker films to ensure the required insulation quality, and this is against the general trend toward miniaturization. On the other hand, in Al_2O_3 films, although the band gap (6.7 eV) and CBO (1.6 eV) are smaller than those of SiO_2 [24], the gate leakage current can be reduced due to the large dielectric constant ($\epsilon = 8.5$). However, it has been reported that the formation of Al_2O_3 at the fabrication temperature causes its crystallization and the generation of grain boundaries, resulting in an increase in the gate leakage current [25,26], presumably due to the resulting current through the grain boundaries.

To make use of the advantages and compensate for the disadvantages of SiO_2 and Al_2O_3 films, the use of amorphous $(\text{Al}_2\text{O}_3)_{1-x}(\text{SiO}_2)_x$ mixed oxides may be a solution [24,27]. Those oxides are not new materials. They have been studied in the fields of geoscience and materials science, and their structures have been analyzed by several experimental techniques such as nuclear magnetic resonance, infrared spectroscopy, and x-ray scattering, as well as by theoretical calculations [28–34]. Recently, in the context of the development of GaN-based MOSFETs, high-quality amorphous gate oxides $(\text{Al}_2\text{O}_3)_{1-x}(\text{SiO}_2)_x$ have been fabricated by alternate deposition of SiO_2

and Al_2O_3 layers on GaN followed by annealing at a sufficiently high temperature [24,27]. Control of the thickness of the deposited layers enables one to form $(\text{Al}_2\text{O}_3)_{1-x}(\text{SiO}_2)_x$ with any value of x . The resulting GaN-based MOS devices with $(\text{Al}_2\text{O}_3)_{1-x}(\text{SiO}_2)_x$ gate oxides indeed show good performance [24,27]. X-ray photoemission spectroscopy shows that the band gap and thus the CBO and VBO increase when the amount of Si in the $(\text{Al}_2\text{O}_3)_{1-x}(\text{SiO}_2)_x$ is increased [24], as schematically shown in Fig. 1. Crystallization and the formation of grain boundaries are also suppressed when the amount of Si is increased. On the other hand, the dielectric constant increases with an increasing amount of Al. Namely, $(\text{Al}_2\text{O}_3)_{1-x}(\text{SiO}_2)_x$ has a larger band offset and a higher crystallization temperature than Al_2O_3 , and has a larger dielectric constant than SiO_2 , possibly resulting in a high breakdown field in GaN-based MOS devices. Moreover, $C-V$ measurements of a GaN-based MOS capacitor with an $(\text{Al}_2\text{O}_3)_{1-x}(\text{SiO}_2)_x$ gate oxide shows a lower interfacial defect density than that for a SiO_2 gate oxide [27]. Hence, it is now recognized that, considering its dielectric constant and the band offset, $(\text{Al}_2\text{O}_3)_{1-x}(\text{SiO}_2)_x$ with a suitable choice of x is intrinsically the most promising gate insulator for GaN-based MOS devices.

The remaining important characteristic among the three stated earlier is the defects in $(\text{Al}_2\text{O}_3)_{1-x}(\text{SiO}_2)_x$. It is necessary to clarify the nature of the point defects that occur and their effects on the gate leakage current. Many theoretical calculations have been performed to reveal the structures and characteristics of point defects in SiO_2 and Al_2O_3 [35–49]. In particular, first-principles calculations based on density-functional theory (DFT) [50,51] performed for SiO_2 have made it clear that the oxygen vacancy (V_O) in SiO_2 , which is the most typical point defect in that system, exhibits structural bistability associated with carrier trapping [36,38–40]. This is regarded as being responsible for the electric-stress-induced leakage current (SILC) in Si-based MOS devices [37]. In the case of amorphous Al_2O_3 , oxygen vacancies are reported to be assimilated into the amorphous network [47].

Oxygen vacancies are generally the most abundant point defects in oxides. However, knowledge as to the atomic structure, energetics, and electronic structure of V_O in $(\text{Al}_2\text{O}_3)_{1-x}(\text{SiO}_2)_x$ mixed oxides is insufficient, although some theoretical calculations of the structural and dynamical properties of the host oxides are available [29,32,33]. Previous theoretical studies have reported the structure of $(\text{Al}_2\text{O}_3)_{1-x}(\text{SiO}_2)_x$ for particular compositions, mainly using empirical potentials [29,32], and have not addressed structural variations as a function of the composition x . Reliable calculations for oxygen vacancies based on quantum theory are very much needed. The purpose of the present paper is to respond this need.

Based on DFT, we prepare amorphous $(\text{Al}_2\text{O}_3)_{1-x}(\text{SiO}_2)_x$ with 11 different compositions x ($x = 0.00, 0.07,$

0.15, 0.22, 0.30, 0.37, 0.44, 0.52, 0.59, 0.67, and 1.00) by the melt-quench method and then determine the atomic and electronic structures and the energetics of all possible neutral oxygen vacancies in these mixed oxides. We find that the energetically favorable neutral V_O in $(\text{Al}_2\text{O}_3)_{1-x}(\text{SiO}_2)_x$ induces no deep levels in the mid-gap region of GaN and is unlikely to be the origin of the leakage current, thus indicating that $(\text{Al}_2\text{O}_3)_{1-x}(\text{SiO}_2)_x$ is the best candidate at present for gate oxides in GaN technology.

The organization of the present paper is as follows. In Sec. II, we explain the calculational method and the melt-quench scheme used to form the $(\text{Al}_2\text{O}_3)_{1-x}(\text{SiO}_2)_x$ mixed oxides. In Sec. III A, we show the atomic and electronic structures obtained and the energetics of V_O . In Sec. III B, we determine the pathways and corresponding energy barriers for the structural transformations among the various V_O 's, and identify stable and electronically inactive V_O 's in $(\text{Al}_2\text{O}_3)_{1-x}(\text{SiO}_2)_x$ mixed oxides. Section IV summarizes our findings.

II. CALCULATIONS

A. Methods

All the calculations are performed using DFT with the Kohn-Sham scheme [51] using the Vienna *ab initio* simulation package (VASP) [52,53]. For the exchange-correlation functional, we use the generalized gradient approximation (GGA) of Perdew, Burke, and Ernzerhof [54] in order to perform molecular-dynamics calculations and structural optimization. To obtain more accurate energy levels of V_O , the hybrid functional proposed by Hyde, Scuseria and Ernzerhof (HSE) [55] is used to calculate the density of states. We set the fraction of Fock exchange and the range-separation parameter in the HSE functional to 0.35 and 0.20 Å⁻¹, respectively, which produces a band gap of 8.7 eV for $\alpha\text{-Al}_2\text{O}_3$ (5% smaller than the experimental value). Interactions between the ionic cores and the valence electrons are described by the projector-augmented-wave potential [56]. The electron wave functions (Kohn-Sham orbitals) are expanded using plane waves up to a kinetic energy of 400 eV, which suffices to ensure an accuracy of 30 meV in the defect formation energy. The effects of spin polarization are examined by taking oxygen vacancies in $(\text{Al}_2\text{O}_3)_{1-x}(\text{SiO}_2)_x$ as examples and are found to be minor (see Sec. III A). A defect in an amorphous material is simulated by a supercell model with dimensions of 12.99–14.28 Å (see Sec. II B). Hence Γ -point sampling for integration over the Brillouin zone is enough for the present supercell model. Structural optimization is performed until all the atomic forces are less than 0.01 eV/Å.

In order to assess the accuracy of the present calculations, we first calculate the structural parameters of crystalline $\alpha\text{-Al}_2\text{O}_3$ and $\alpha\text{-SiO}_2$ with hexagonal lattices.

The lattice constants obtained for $\alpha\text{-Al}_2\text{O}_3$ are $a = b = 4.81$ Å and $c = 13.12$ Å, and the bulk modulus obtained is 227.7 GPa. These values agree with the experimental values with an error of 1.00%–1.05% in the lattice constants [57] and 10.2% in the bulk modulus [58]. The values obtained for $\alpha\text{-SiO}_2$ are $a = b = 5.00$ Å, $c = 5.55$ Å, and 36.5 GPa, respectively. These agree with the experimental values with an error of 1.71%–2.68% in the lattice constants [59] and 3.2% in the bulk modulus [60]. Structural properties of other polymorphs of SiO_2 (cristobalite and stishovite) are also computed and are found to agree with the experimental values to within several percent. Secondly, we take the example of the oxygen vacancy V_O in $\alpha\text{-SiO}_2$. It is known that V_O shows a bistable structure, i.e., it can have a dimerized Si—Si structure or a puckered structure [36,38]. We indeed find this bistability, and the total-energy difference obtained is 3.0 eV for the neutral V_O , which agrees with the value of 3.1 eV obtained in the past [38]. Thirdly, we consider V_O in $\alpha\text{-Al}_2\text{O}_3$ and calculate the energy gain due to the relaxation of surrounding atoms. The energy gain obtained after the relaxation of 16 surrounding atoms is 0.09 eV, which again agrees with the value of 0.09 eV obtained in the past [41]. The VESTA system is used to draw the atomic configurations [61].

B. Models and melt-quench technique for amorphous materials

To describe defects in amorphous $(\text{Al}_2\text{O}_3)_{1-x}(\text{SiO}_2)_x$, we adopt hexagonal supercell models. The dimensions of the supercells are fixed at $a = b = 14.28$ Å and $c = 12.99$ Å, which correspond to the experimental values for $\alpha\text{-Al}_2\text{O}_3$ [57]. Consequently, our supercell for Al_2O_3 contains 108 Al and 162 O atoms, the density being 3.99 g/cm³. Using these experimental lattice parameters, the calculated bulk modulus of $\alpha\text{-Al}_2\text{O}_3$ is 228.3 GPa, which agrees with our theoretical value of 227.7 GPa mentioned in the previous section within an accuracy of 0.2%. The density of amorphous Al_2O_3 shows a distribution with a range of 3.05–3.40 g/cm³ in experimental measurements [62,63]. We prepare the $(\text{Al}_2\text{O}_3)_{1-x}(\text{SiO}_2)_x$ system by removing $n(\text{Al}_2\text{O}_3)$ units from the supercell (i.e., $\text{Al}_{108}\text{O}_{162}$) and adding $n(\text{SiO}_2)$ units, leading to $(\text{Al}_2\text{O}_3)_{1-x}(\text{SiO}_2)_x$ with $x = n/54$. The density of SiO_2 in our fixed-volume supercell model then becomes 2.35 g/cm³. The density of amorphous SiO_2 is about 2.20 g/cm³, and the density of crystalline $\alpha\text{-SiO}_2$ is 2.6 g/cm³. Hence the density of SiO_2 in our model is in the range of that of the target material, although further volume optimization for each value of x in the calculations may provide more accurate results. We restrict ourselves in this paper to some salient features of defects that are insensitive to the density of amorphous $(\text{Al}_2\text{O}_3)_{1-x}(\text{SiO}_2)_x$.

In order to form amorphous materials in our calculations, we adopt the melt-quench technique using molecular dynamics (MD) based on density-functional theory, i.e., the target system is heated to a temperature well above the melting temperature to erase the memory of the initial structure and then quenched to room temperature at a slow enough speed to avoid fictitious defects in the resultant amorphous material. This melt-quench technique has been used extensively to investigate amorphous materials, in particular amorphous SiO_2 [43,64–67], with classical force-field Lagrangians or a density-functional Lagrangian. Two central issues in preparing the amorphous material are the size of the supercell model and the quenching rate. The classical-field Lagrangians have obvious advantages in that they allow one to use larger supercells and slower quenching rates, although the validity of these Lagrangians needs to be examined, whereas the density-functional Lagrangian is capable of describing the properties of condensed matter accurately. With classical MD, the effects of the quenching speed on the structural properties of amorphous SiO_2 have been carefully examined [43,64,67], with the slowest rate being 5 K/ns [67]. The effects of the supercell size have also been examined, using a supercell consisting of 13 824 atoms [67]. On the

other hand, with density-functional MD, the largest cell size ever used is 192 atoms, and the slowest quenching rate is 250 K/ps [66]. Nevertheless, the results obtained by such density-functional MD reproduce the static structure factor of amorphous SiO_2 [66]. Hence, in this study we form our amorphous $(\text{Al}_2\text{O}_3)_{1-x}(\text{SiO}_2)_x$ mixed oxides by the melt-quench technique in Born-Oppenheimer MD simulations using DFT with a quenching rate of 200 K/ps and a supercell size of 162–270 atoms. Results obtained with a slower quenching rate of 100 K/ps are also used for comparison (see below).

Experimental studies have reported that $(\text{Al}_2\text{O}_3)_{1-x}(\text{SiO}_2)_x$ shows more durability in its breakdown properties under Al-rich conditions, with an optimum value of $x = 0.347$ [27]. Thus, in this paper, we focus mainly on Al-rich stoichiometries and examine 11 cases, i.e., $x \approx 0.00, 0.07, 0.15, 0.22, 0.30, 0.37, 0.44, 0.52, 0.59, 0.67$, and 1.00. For each stoichiometry, we make a single amorphous sample. To prepare the initial structure of $(\text{Al}_2\text{O}_3)_{1-x}(\text{SiO}_2)_x$ ($x = n/54$), we randomly remove $2n$ Al atoms and n O atoms and then put n Si atoms at the Al sites, again randomly. For the initial structure of SiO_2 , we place 54 Si atoms and 108 O atoms randomly. Each system with a particular value of x is then heated up to

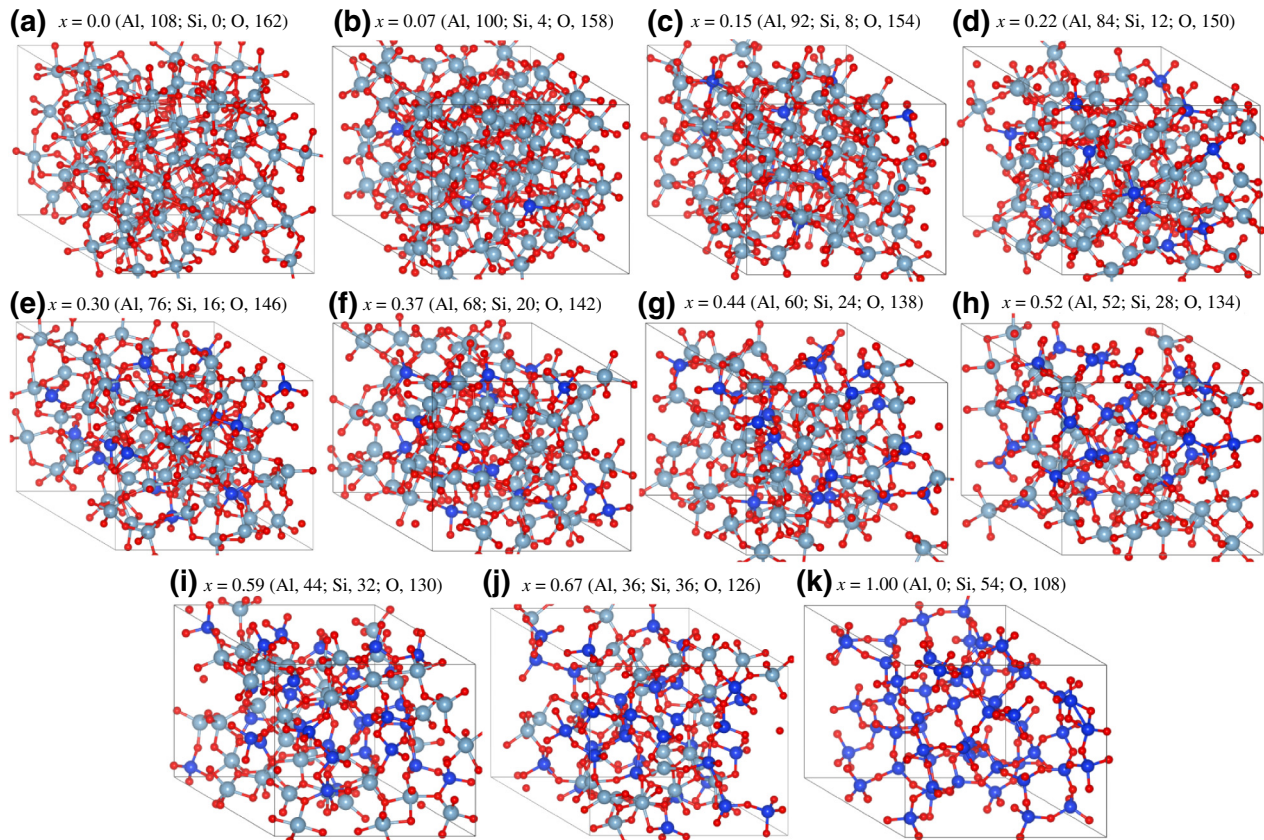


FIG. 2. Atomic structures of amorphous $(\text{Al}_2\text{O}_3)_{1-x}(\text{SiO}_2)_x$ mixed oxides obtained by the present melt-quench method for each value of x considered. The numbers of each atomic species in the simulation cell are also shown. Silver, blue, and red spheres represent Al, Si, and O atoms, respectively.

TABLE I. Coordination number of each atomic species in amorphous $(\text{Al}_2\text{O}_3)_{1-x}(\text{SiO}_2)_x$ mixed oxides obtained by the melt-quench method.

x	0.00	0.07	0.15	0.22	0.30	0.37	0.44	0.52	0.59	0.67	1.00
Al	5.47	5.51	5.32	5.20	5.01	5.04	4.93	4.83	4.66	4.72	
Si		4.50	4.63	4.58	4.25	4.15	4.08	4.07	4.09	4.03	4.00
O	3.86	3.79	3.55	3.44	3.23	3.14	2.95	2.80	2.65	2.54	2.00

6000 K, well above the melting temperature, and equilibrated for 10 ps; it is confirmed that it is in the melt phase. Then, the system is quenched to 0 K at a rate of 200 K/ps. Finally, a structural optimization is performed at 0 K. The amorphous structures thus obtained are presented in Fig. 2.

We find that the calculated energy spectra (Kohn-Sham-level structures) show clear gaps without deep levels for all the 11 amorphous $(\text{Al}_2\text{O}_3)_{1-x}(\text{SiO}_2)_x$ materials. One typical structural imperfection in SiO_2 is an undercoordinated Si atom (a dangling bond), which induces a deep level in the gap [38,40]. Hence the absence of deep levels observed in our amorphous samples for SiO_2 and also for $(\text{Al}_2\text{O}_3)_{1-x}(\text{SiO}_2)_x$ with larger values of x indicates that there are no undercoordinated Si atoms in those samples. The definition of a dangling bond in Al_2O_3 is more ambiguous, since Al_2O_3 is much more ionic than SiO_2 . However, the coordination number provides a sign of structural imperfections. Table I shows the calculated coordination numbers of each atomic species in amorphous $(\text{Al}_2\text{O}_3)_{1-x}(\text{SiO}_2)_x$. The values are averaged over all the corresponding atoms in the sample. Here, the coordination number of an Al or the Si atom is defined as the number of nearby O atoms, and that of an O atom as the number of nearby Al plus Si atoms. The threshold values for the nearby distances are set at 2.3 and 1.9 Å for Al—O and Si—O bonds, respectively. In our amorphous SiO_2 , the coordination numbers are 4.0 and 2.0 for Si and O, respectively, corroborating the absence of undercoordinated Si atoms. In our amorphous Al_2O_3 , the average coordination numbers are 5.47 and 3.86 for Al and O, respectively. These values are close to the

corresponding values of 6 and 4 for crystalline $\alpha\text{-Al}_2\text{O}_3$ [57], indicating that structural imperfections that could cause deep levels are unlikely. This is in accord with the Kohn-Sham-level structure obtained. We find that the coordination numbers of O and Al decrease almost monotonically with increasing x , whereas the coordination number of Si is in the range between 4.0 and 4.5. Our amorphous materials have tail states in the energy gap, as is evidenced by the narrowing of the calculated energy gap: 8.7 and 6.5 eV for $\alpha\text{-Al}_2\text{O}_3$ and amorphous Al_2O_3 , respectively, and 8.8 and 7.9 eV for $\alpha\text{-SiO}_2$ and amorphous SiO_2 , respectively. These tail states in the amorphous materials presumably come from bond networks that are different from those in the corresponding crystalline materials.

Another important quantity is the structural correlation function. Figure 3 shows calculated partial pair correlation functions of Si-O, Si-Si, and O-O pairs in amorphous SiO_2 ($x = 1.00$). The first peaks are prominent and are located at 1.63 Å for Si-O pairs, at 2.98 Å for Si-Si pairs, and at 2.62 Å for O-O pairs. The second peaks are much less prominent (this is typical of an amorphous structure), and are located at 4.18 Å for Si-O pairs, at 4.98 Å for Si-Si pairs, and at 5.13 Å for O-O pairs. These peak positions, especially for the first peak, are in agreement with those obtained in previous LDA-based molecular-dynamics calculations [66]. Furthermore, in Fig. 3, we show the pair correlation function for amorphous SiO_2 obtained from our calculations with a slower quenching rate, 100 K/ps. The results obtained for the two rates, 200 K/ps and 100 K/ps, are essentially the same, showing the suitability of our melt-quench scheme.

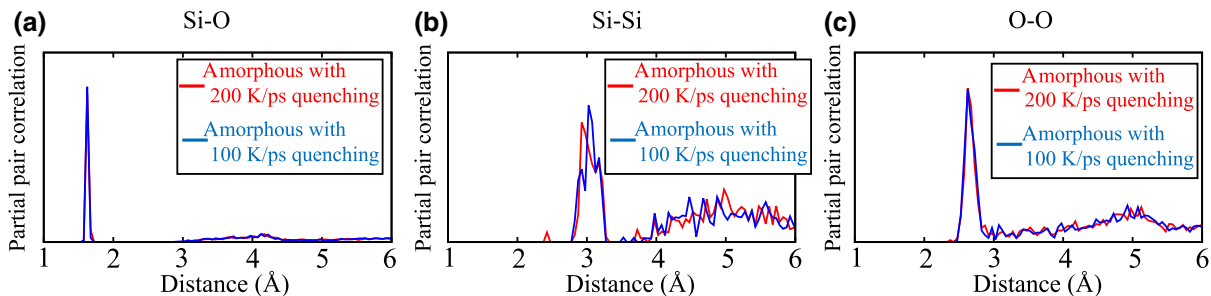


FIG. 3. Calculated partial pair correlation functions of (a) Si-O, (b) Si-Si, and (c) O-O pairs in amorphous SiO_2 with quenching rates of 200 and 100 K/ps.

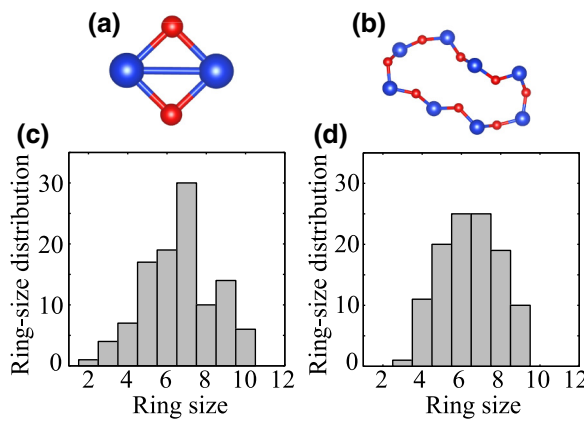


FIG. 4. Examples of ring networks in amorphous SiO₂. (a) Two-membered and (b) eight-membered ring structures. The blue and red spheres depict Si and O atoms, respectively. (c),(d) Ring-size distributions for amorphous SiO₂ obtained with quenching rates of (c) 200 K/ps and (d) 100 K/ps.

The ring-size distribution in amorphous SiO₂, where the ring size is defined by the number of Si atoms constituting the ring, is an interesting quantity for characterizing the amorphous structure. It has been reported that amorphous SiO₂ has a wide distribution of ring sizes, although α -SiO₂ has only six-membered and eight-membered rings [65]. The amorphous SiO₂ that we obtain also shows a wide distribution, from two-membered to ten-membered rings, in which seven-membered rings are the most abundant (Fig. 4). Although the two-membered ring has been suspected to be a network artifact induced by small cell sizes or fast quenching rates [65], its existence has been reported even in calculations with larger cell sizes or slower quenching rates [66]. Two-membered rings appear in our calculation also. Further efforts are required to obtain definite ring statistics.

C. Defects in supercell models

To simulate an oxygen vacancy V_O in an infinite-size amorphous material, we use a supercell model in which each V_O is placed in a large enough atomic system to represent the amorphous material, and the atomic system is arranged periodically. We prepare a single amorphous sample of mixed amorphous (Al₂O₃)_{1-x}(SiO₂)_x for each value of x. However, the configuration of V_O in each sample of (Al₂O₃)_{1-x}(SiO₂)_x is statistically diverse: e.g., in our amorphous Al₂O₃, there are 162 distinct O sites, thus leading to 162 distinct V_O's. We perform structural optimization and calculate formation energies for all the possible V_O's in each (Al₂O₃)_{1-x}(SiO₂)_x.

The modeling of point defects by supercells is accompanied by an obvious drawback caused by finite-size effects. Lipmann-Schwinger schemes [68–70] may be less affected

by finite-size effects. In the present paper, we find that neutral oxygen vacancies with low formation energies induce no deep levels in the GaN energy gap (Sec. III A), suggesting that the roles of charged states are minor. We thus focus on the neutral V_O in this paper, and neglect corrections due to finite size [42,71–74].

III. RESULTS

A. Formation energy and electron states of oxygen vacancy

In this study, we focus on the neutral oxygen vacancy V_O. The formation energy E_{form} of V_O in (Al₂O₃)_{1-x}(SiO₂)_x is an appropriate quantity for judging its stability and abundance. We calculate E_{form} from

$$E_{\text{form}} = E_{V_O} - E_{(\text{Al}_2\text{O}_3)_{1-x}(\text{SiO}_2)_x} - \mu_O, \quad (1)$$

where E_{(Al₂O₃)_{1-x}(SiO₂)_x} and E_{V_O} are the total energies of the vacancy-free amorphous structure and the structure with a single V_O, respectively, and μ_O is the chemical potential of oxygen, for which we take half the energy of an O₂ molecule in this paper. As explained in Sec. II B, our supercell model for (Al₂O₃)_{1-x}(SiO₂)_x contains 108 – 2n Al, n Si, and 162 – n oxygen atoms ($x = n/54$), and all the O sites are distinct from each other. We thus remove an oxygen atom from each of the possible sites (162 – n sites) in our amorphous (Al₂O₃)_{1-x}(SiO₂)_x to form an oxygen monovacancy V_O and then perform structural optimization for all of the 162 – n possible configurations. We repeat this procedure for five representative values of x, i.e., x=0.00, 0.30, 0.44, 0.67, and 1.00. Our calculations thus cover the variability of the structures and formation energies of V_O in amorphous (Al₂O₃)_{1-x}(SiO₂)_x.

The minimum, maximum, and average values of the formation energy of V_O obtained are shown in Table II for each value of x. We find that the minimum and maximum values are almost independent of the value of x (the Si composition). However, we find a clear trend in which the average value of the formation energy decreases with increasing x. To reveal the reason for this trend, we examine the neighboring atoms surrounding the V_O and classify all the V_O's in terms of the number i of neighboring Al atoms, labeling them as V_O-Al(i). The averages of the calculated formation energies for each class V_O-Al(i), denoted by E_{form}^{V_O-Al(i)}, are shown in Table II. We find that the average formation energy of V_O-Al(i) decreases with decreasing i in the range 4.9–6.7 eV. The lowest average formation energy is obtained for V_O-Al(0), the vacancy in which the annihilated O atom is originally connected to only Si atoms. When x increases, the ratio of Si to Al increases so that the numbers of configurations of V_O-Al(i) with a smaller i increase. This is the reason for the observed decreasing trend in the average formation energy with increasing x.

TABLE II. Minimum ($E_{\text{form}}^{\text{Min}}$), maximum ($E_{\text{form}}^{\text{Max}}$), and average ($E_{\text{form}}^{\text{Ave}}$) values of the formation energies of an oxygen monovacancy V_O in amorphous $(\text{Al}_2\text{O}_3)_{1-x}(\text{SiO}_2)_x$, in units of eV. $E_{\text{form}}^{V_O-\text{Al}(i)}$ is the average value of the formation energy in the case where an O atom with i Al—O bonds is removed to form a V_O in the $(\text{Al}_2\text{O}_3)_{1-x}(\text{SiO}_2)_x$ (eV).

Model	$E_{\text{form}}^{\text{Min}}$	$E_{\text{form}}^{\text{Max}}$	$E_{\text{form}}^{\text{Ave}}$	$E_{\text{form}}^{V_O-\text{Al}(0)}$	$E_{\text{form}}^{V_O-\text{Al}(1)}$	$E_{\text{form}}^{V_O-\text{Al}(2)}$	$E_{\text{form}}^{V_O-\text{Al}(3)}$	$E_{\text{form}}^{V_O-\text{Al}(4)}$	$E_{\text{form}}^{V_O-\text{Al}(5)}$
$x = 0.00$	4.5	7.3	6.4	—	—	—	6.1	6.5	6.7
$x = 0.30$	4.6	7.2	6.3	4.9	5.5	6.0	6.5	6.7	—
$x = 0.44$	5.0	7.2	6.2	5.3	5.7	6.1	6.5	6.7	—
$x = 0.67$	4.7	7.0	5.9	5.6	5.8	6.1	6.5	6.6	—
$x = 1.00$	4.8	6.5	5.7	5.7	—	—	—	—	—

To discuss the electronic energy levels in the energy gap, we use the calculated Kohn-Sham-level positions in this paper. These are obviously an approximation to the (q/q') occupancy level, the Fermi-level position at which the total energies of the charge states q and q' become equal [75,76] and thus carrier capture takes place. To examine the validity and limitations of this approximation, we calculate the Kohn-Sham levels induced by more than a hundred various V_O 's in our amorphous SiO₂. The levels obtained by GGA calculations are distributed around the center, 0.42 eV above the valence-band maximum (VBM) of amorphous SiO₂, with a half-width of 0.4 eV. This result is comparable to that of previous occupancy-level calculations using the GGA, in which the levels are distributed around about 0.5 eV above the VBM of amorphous SiO₂ [44]. As for V_O in amorphous Al₂O₃, the Kohn-Sham levels in the 162 distinct V_O 's obtained are distributed around 1.4 eV, with a half-width of above 1.0 eV, above the VBM of our amorphous Al₂O₃. The (0/+1) occupancy levels induced by a V_O in crystalline α -Al₂O₃ are reported to be at about 2.5 eV above the VBM of the α -Al₂O₃ from GGA calculations [42]. Our Kohn-Sham-level positions for V_O in amorphous Al₂O₃ are lower than the occupancy-level positions previously obtained for α -Al₂O₃, although the VBM of our amorphous Al₂O₃ is shifted upward substantially compared with that of α -Al₂O₃. Considering these results, the features of the Kohn-Sham levels obtained in the present study are likely to reflect the features of the occupancy-level structures.

We are now in a position to show the geometric and electronic structures of V_O in $(\text{Al}_2\text{O}_3)_{1-x}(\text{SiO}_2)_x$. We examine the cases of $x = 0.30, 0.44, 0.59$, and 0.67 . The results obtained are essentially the same in the four cases. Hence we show the results for $(\text{Al}_2\text{O}_3)_{0.70}(\text{SiO}_2)_{0.30}$ (i.e., $n = 16$), in which there are 146 distinct oxygen vacancies. We focus here on the V_O 's with the highest and lowest formation energies to clarify the salient features of the oxygen vacancies in $(\text{Al}_2\text{O}_3)_{0.70}(\text{SiO}_2)_{0.30}$. The V_O with the highest formation energy, 7.2 eV, is formed at an O site with three nearest-neighbor Al atoms. (This V_O has a higher formation energy than the average formation energy $E_{\text{form}}^{V_O-\text{Al}(4)}$ shown in Table II.) This local configuration of a single O

atom and three Al atoms is substantially ionic. Hence, after removal of the O atom, the electron state originating from the neighboring Al atoms and located near the conduction-band edge shifts downwards to appear as a deep level. Our HSE calculation indeed makes it clear that a deep Kohn-Sham level appears at 1.9 eV above the VBM in our amorphous $(\text{Al}_2\text{O}_3)_{0.70}(\text{SiO}_2)_{0.30}$ [Fig. 5(a)]. We also examine the Kohn-Sham levels of other oxygen vacancies using the GGA. We find that most of the oxygen vacancies with higher formation energies (more than 6.1 eV) induce deep Kohn-Sham levels distributed over a width of 0.5 eV. The characters of these deep levels are found to be those of the neighboring Al atoms. Considering that the band offset of our $(\text{Al}_2\text{O}_3)_{0.70}(\text{SiO}_2)_{0.30}$ with respect to GaN is about 1.7 eV, these Kohn-Sham levels are located in the lower half of the band gap of GaN. The atomic structures of the V_O 's with higher formation energies are also observed as typical structures of V_O in our amorphous Al₂O₃. Hence,

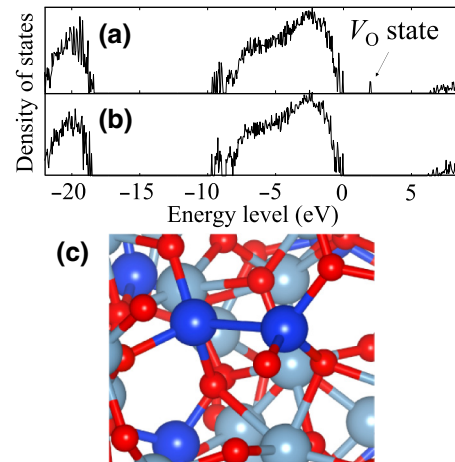


FIG. 5. (a),(b) Density of states of the $(\text{Al}_2\text{O}_3)_{0.70}(\text{SiO}_2)_{0.30}$ mixed oxide containing a single oxygen vacancy V_O obtained by use of the HSE functional, (a) with the largest formation energy and (b) with the smallest formation energy. The origin of the energy is set at the valence-band maximum. (c) Atomic structure of V_O with the smallest formation energy. A Si—Si bond is formed after removal of the oxygen atom. Silver, blue, and red spheres represent Al, Si, and O atoms, respectively.

we use the generic label $V_O^{Al_2O_3}$ for these oxygen vacancies from now on.

On the other hand, the V_O with the lowest formation energy is formed at an O site with two Si—O bonds and no Al—O bonds. Our HSE calculation shows that removal of the O atom from this site induces no Kohn-Sham level in the energy gap of $(Al_2O_3)_{0.70}(SiO_2)_{0.30}$ [Fig. 5(b)]. The coordination numbers of the two nearest-neighbor Si atoms are unchanged even after the O atom is removed, due to Si—Si rebonding [Fig. 5(c)]. The covalency in the local Si—O—Si configuration is important for such rebonding. Si—Si rebonding is also observed in SiO_2 and induces energy levels above the VBM and below the conduction-band minimum of SiO_2 [35,44]. However, these levels are located in the valence and conduction bands of $(Al_2O_3)_{1-x}(SiO_2)_x$ due to its narrower band gap than that of SiO_2 . We also examine the other oxygen vacancies with lower formation energies using the GGA. As stated above, in such vacancies one or two Si atoms, in addition to Al atoms, surround the V_O . We observe weak rebonding among those atoms, with bond lengths $d_{Si-Si} \approx 3.0 \text{ \AA}$ and $d_{Si-Al} \approx 2.6 \text{ \AA}$. We find that the majority of the oxygen vacancies with lower formation energies (less than 5.7 eV) generate Kohn-Sham levels in the valence band or, at the highest, 0.5 eV above the VBM of $(Al_2O_3)_{0.70}(SiO_2)_{0.30}$. Considering the band offset at the $(Al_2O_3)_{1-x}(SiO_2)_x/GaN$ interface, the energy levels induced by the oxygen vacancies with lower formation energies do not appear in the GaN band gap in $(Al_2O_3)_{1-x}(SiO_2)_x/GaN$ MOS structures. Since the characteristics of the atomic structure (Si—Si rebonding) and the energy levels of the Si-surrounded oxygen vacancies are common to those of oxygen vacancies in SiO_2 [35,44], we use the generic label $V_O^{SiO_2}$ for these oxygen vacancies from now on.

The tendency for the levels induced by the oxygen vacancies with lower formation energy, i.e., those which are surrounded by more Si atoms, to be located outside the GaN band gap, and for the levels induced by the V_O 's with higher formation energy, i.e., those which are surrounded by more Al atoms, to be located in the GaN band gap is demonstrated by our calculations shown in Fig. 6. Although the distribution of the KS levels induced by the distinct V_O 's in the amorphous structure is somewhat diverse, we can see the tendency clearly. Essentially the same results are obtained for other values of x . Hence it is likely that the oxygen vacancies with lower formation energy in $(Al_2O_3)_{1-x}(SiO_2)_x$ induce no deep levels in the GaN band gap, even if they do so in the gap of the oxide itself. The absence of deep levels caused by oxygen vacancies that have a low formation energy implies a lesser importance of charged V_O 's generated by capture of carriers. We thus focus on the neutral V_O in this paper.

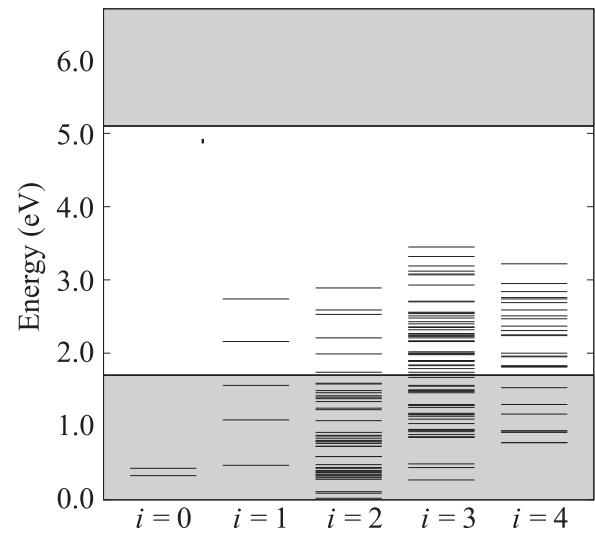


FIG. 6. Distribution of Kohn-Sham (KS) levels induced by V_O in amorphous $(Al_2O_3)_{0.70}(SiO_2)_{0.30}$. The short lines depict the positions of the KS levels induced by $V_O-Al(i)$ with $i = 0, 1, 2, 3$, and 4. Each distinct V_O usually induces a single KS level, and its distribution among the different V_O 's is shown in the energy gap of $(Al_2O_3)_{0.70}(SiO_2)_{0.30}$ (approximately 6.7 eV), denoted by the top and bottom solid horizontal lines. The calculated KS levels are obtained by the GGA and then adjusted so that they are aligned with the experimental band offsets [24]. The energy regions outside the band gap of GaN (3.4 eV) are shaded in gray.

It is noteworthy that the highest occupied levels for the oxygen vacancies examined here are found to be doubly occupied without degeneracy. This situation is like a closed-shell electron configuration and is presumably peculiar to ionic materials. Hence a spin polarization due to localized electrons is unlikely. We indeed find no spin-polarized solutions of the Kohn-Sham equation for various V_O in $(Al_2O_3)_{1-x}(SiO_2)_x$.

The calculated formation energy depends on the oxygen chemical potential. The present choice of μ_O corresponds to an O-rich condition. In O-poor conditions in which Al or Si is precipitated, μ_O is lower than the present choice by more than several eV [77]. Then, in a harsh environment such as that which can occur during device operation, it is possible for oxygen vacancies to be formed. However, such V_O 's are expected to be mainly $V_O-Al(0)$ from our formation-energy calculations, and no deep levels should appear in the GaN band gap; thus, oxygen vacancies are not responsible for the degradation of MOS devices reflected in effects such as SILC.

Recent molecular-dynamics simulations based on density-functional theory for the neutral oxygen vacancy in amorphous Al_2O_3 show an interesting structural relaxation leading to assimilation of the vacancy into the amorphous structure [47]. We do not find such assimilation, presumably because there is a certain energy barrier to the

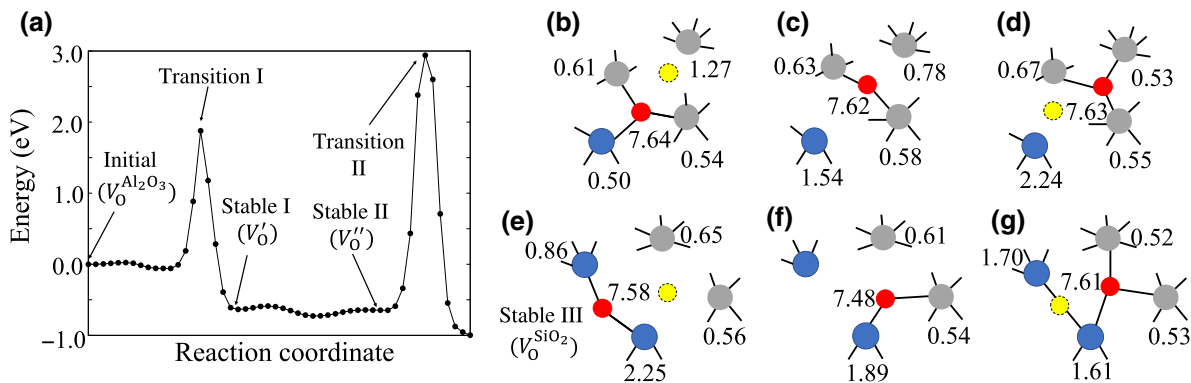


FIG. 7. (a) Calculated energy profile along the first pathway from $V_O^{Al_2O_3}$ to $V_O^{SiO_2}$ in the $(Al_2O_3)_{0.33}(SiO_2)_{0.67}$ mixed oxide. (b)–(g) Schematic view of the pathway obtained: (b) initial state, (c) transition state I, (d) stable state I, (e) stable state II, (f) transition state II, and (g) stable state III. The numbers inserted next to the atoms are the numbers of valence electrons around each atom obtained by Bader charge analysis. Gray, blue, red, and yellow filled circles represent Al atoms, Si atoms, O atoms, and V_O defects, respectively.

assimilation of the vacancy structure. Further investigation is required to reveal the details of such assimilation.

B. Structural transformations of oxygen vacancies

In the previous section, we determine the structures and formation energies of various oxygen vacancies in amorphous $(Al_2O_3)_{1-x}(SiO_2)_x$. It is found that oxygen vacancies surrounded by more Si atoms are lower in formation energy than those surrounded by Al atoms. The concentration of each type of oxygen vacancy depends on the formation energy, so that it varies from its lowest value (that of $V_O^{Al_2O_3}$) to its highest value (that of $V_O^{SiO_2}$). However, oxygen vacancies that induce deep levels may exist in as-deposited amorphous $(Al_2O_3)_{1-x}(SiO_2)_x$. Thermal annealing, which is a usual process in the fabrication of electron devices, may decrease the concentrations of those vacancies and thus improve the electronic properties of $(Al_2O_3)_{1-x}(SiO_2)_x$ films. In order to examine

such a possibility, we explore in this section the structural transformation between $V_O^{Al_2O_3}$ and $V_O^{SiO_2}$ via the diffusion of oxygen vacancies V_O in $(Al_2O_3)_{1-x}(SiO_2)_x$. The diffusion barrier for neutral V_O in Al_2O_3 and SiO_2 has been reported to be 3.9–6.0 eV and 3.2–5.6 eV, respectively [46,48]. However, the diffusion of neutral V_O in $(Al_2O_3)_{1-x}(SiO_2)_x$ has not been studied. We thus use the nudged-elastic-band method [78–80] to reveal the diffusion pathways and calculate the corresponding energy barriers. We consider $(Al_2O_3)_{1-x}(SiO_2)_x$ with $x = 0.30$ and $x = 0.67$ and explore the reactions in which $V_O^{Al_2O_3}$ is converted to $V_O^{SiO_2}$ via the diffusion of V_O . Note that we consider only the diffusion of neutral V_O in this study. In general, carrier capture, i.e., variation of the charge state, may enhance the diffusivity of defects (recombination-enhanced diffusion) [38, 46,48,81]. Hence, the energy barriers obtained in the following are upper limits for V_O diffusion in each type of $(Al_2O_3)_{1-x}(SiO_2)_x$.

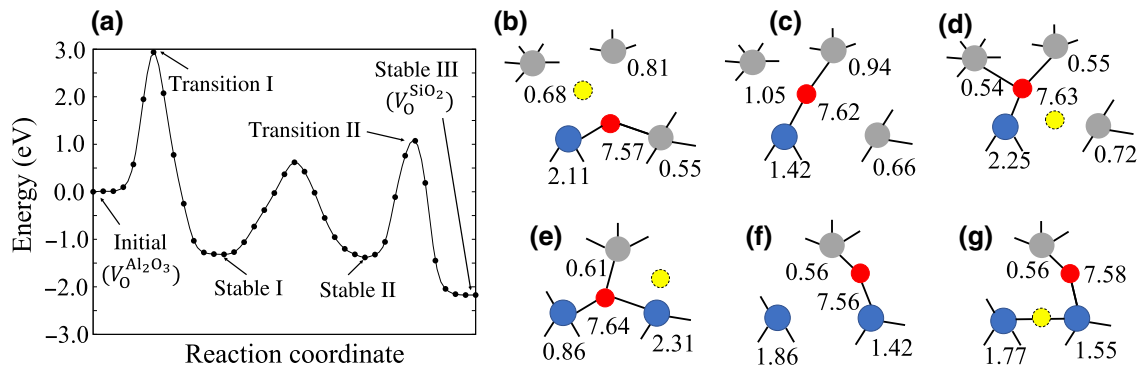


FIG. 8. (a) Calculated energy profile along the second pathway from $V_O^{Al_2O_3}$ to $V_O^{SiO_2}$ in the $(Al_2O_3)_{0.33}(SiO_2)_{0.67}$ mixed oxide. (b)–(g) Schematic view of the pathway obtained: (b) initial state, (c) transition state I, (d) stable state I, (e) stable state II, (f) transition state II, and (g) stable state III. The meaning of the numbers next to the atoms and the color code are the same as in Fig. 7.

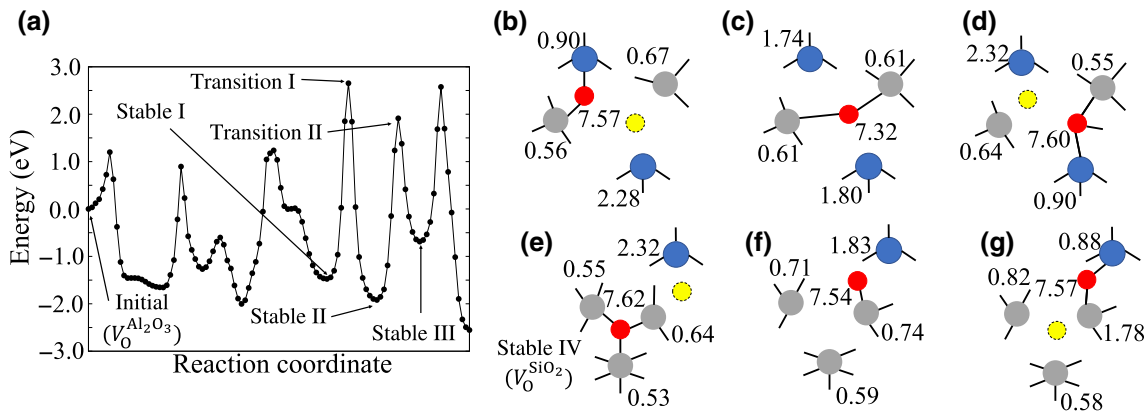


FIG. 9. (a) Calculated energy profile along the first pathway from $V_O^{Al_2O_3}$ to $V_O^{SiO_2}$ in $(Al_2O_3)_{0.70}(SiO_2)_{0.30}$ mixed oxide. (b)–(g) Schematic view of the pathway obtained: (b) stable state I, (c) transition state I, (d) stable state II, (e) stable state II, (f) transition state II, and (g) stable state III. The meaning of the numbers next to the atoms and the color code are the same as in Fig. 7.

In the $(Al_2O_3)_{0.33}(SiO_2)_{0.67}$ mixed oxide, there are several inequivalent $V_O^{Al_2O_3}$ and $V_O^{SiO_2}$ sites. We find two distinct diffusion pathways along which $V_O^{Al_2O_3}$ is converted to $V_O^{SiO_2}$, as shown in Figs. 7 and 8. The numbers inserted next to each atom in Figs. 7 and 8 indicate the numbers of valence electrons around each atom obtained by Bader charge analysis [82,83]. In the initial state of the first pathway, an $-Al-O-Si-$ network exists near the $V_O^{Al_2O_3}$ [Fig. 7(b)]. The $Si-O$ bond in this $-Al-O-Si-$ network is broken first, and transition state I, with a Si dangling bond, appears [Fig. 7(c)]; this is confirmed by the increase in the number of valence electrons on the Si . Then the oxygen atom in the $-Al-O$ structure moves toward the $V_O^{Al_2O_3}$ site, and thus the $V_O^{Al_2O_3}$ is annihilated and another more stable vacancy, V_O' , is formed [stable site I in Fig. 7(d)]. After climbing over some small energy barriers, a $V_O^{Al_2O_3}$ appears near the $-Si-O-Si-$ network

[stable site II in Fig. 7(e)]. One of the $Si-O$ bonds in the nearby $-Si-O-Si-$ network is broken in transition state II [Fig. 7(f)]. Finally, the oxygen atom in the resulting $O-Si-$ structure moves toward the V_O'' vacant site, and a stable configuration is reached [Fig. 7(g)]. This final state is the most stable vacancy, $V_O^{SiO_2}$. Corresponding to the existence of two transition states, the energy profile shows two distinct energy barriers, 1.9 eV and 3.6 eV [Fig. 7(a)].

The energy profile of the second pathway exhibits a similar behavior [Fig. 8(a)]. We find three large energy barriers along the pathway. Two of the three reaction processes for overcoming these large energy barriers are described in Figs. 8(b)–8(g). The first reaction process (initial state to stable state I) is a reaction in which a neighboring oxygen atom moves to the vacant oxygen site through the breaking of a $-Si-O-Al-$ bond, and the third reaction process (stable state II to stable state III) is a reaction in which a

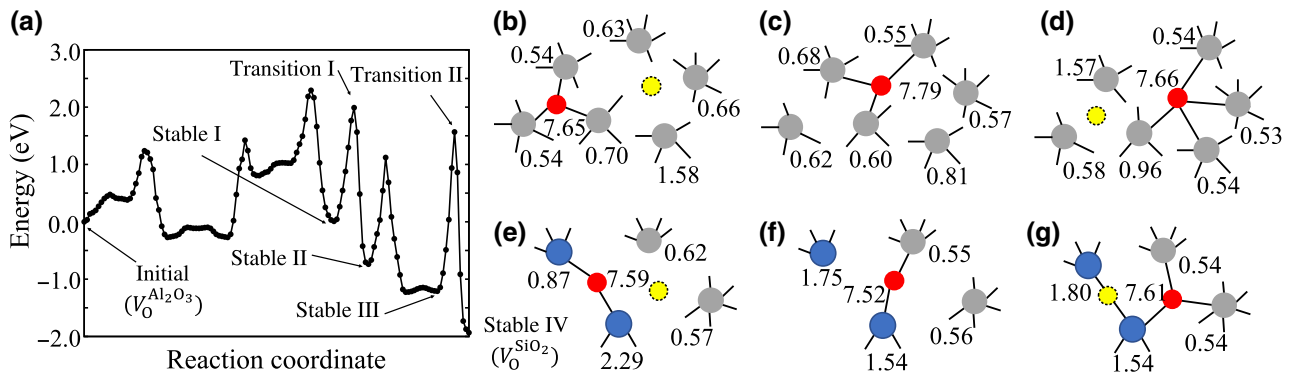


FIG. 10. (a) Calculated energy profile along the second pathway from $V_O^{Al_2O_3}$ to $V_O^{SiO_2}$ in $(Al_2O_3)_{0.70}(SiO_2)_{0.30}$ mixed oxide. (b)–(g) Schematic view of the pathway obtained: (b) stable state I, (c) transition state I, (d) stable state II, (e) stable state III, (f) transition state II, and (g) stable state IV. The meaning of the numbers next to the atoms and the color code are the same as in Fig. 7.

neighboring oxygen atom moves to a vacant oxygen site through the breaking of a Si—O—Si bond. The largest energy barrier is 2.9 eV. Hence, the rate-determining barriers for the transformation from $V_O^{Al_2O_3}$ to $V_O^{SiO_2}$ in the first and the second pathways are 3.6 and 2.9 eV, respectively. These values are generally smaller than the diffusion barriers for V_O in Al_2O_3 and SiO_2 .

For another mixed oxide, $(Al_2O_3)_{0.70}(SiO_2)_{0.30}$, we also find two distinct reaction pathways for the structural transformation from $V_O^{Al_2O_3}$ to $V_O^{SiO_2}$ [Figs. 9 and 10]. The corresponding energy profiles for each pathway show spiky behavior due to the complicated rearrangement of the bonds. In both pathways, a reaction process in which a Si—O bond in a —Si—O—Si or —Si—O—Al—network is broken gives rise to the largest energy barrier, thus being rate-determining. The largest energy barriers in the first and second pathways are 4.1 eV [Fig. 9(a)] and 2.8 eV [Fig. 10(a)], respectively.

In order to further quantify the feasibility of the conversion from $V_O^{Al_2O_3}$ to $V_O^{SiO_2}$, we calculate the occurrence rate f for the reactions above at temperature T , which is given by

$$f = \Gamma \exp(-E_a/k_B T), \quad (2)$$

where Γ is the attempt frequency, E_a is the activation energy, and k_B is the Boltzmann constant. Using transition-state theory [84], the attempt frequency is obtained as

$$\Gamma = \prod_{i=1}^{3N} v_i / \prod_{i=1}^{3N-1} v'_i, \quad (3)$$

where v_i and v'_i are the phonon frequencies of the stable-state and transition-state structures, respectively, and $3N$ is the number of atomic degrees of freedom in the system. By solving the dynamical matrix constructed by shifting the atomic coordinates from either the stable-state or the transition-state geometry, we calculate the phonon frequencies and then the attempt frequency for the barrier-climbing processes in the four distinct reaction pathways presented above. The relevant process in each reaction pathway is the process in which the largest energy barrier is overcome. The calculated occurrence rates for the four reaction pathways are shown in Fig. 11. The calculated attempt frequency for each pathway, along with the relevant energy barrier, is also shown in Fig. 11.

When the relevant energy barrier is smaller than 3.0 eV, the occurrence rate is found to be of the order of $10^{-1} s^{-1}$ even at the lowest temperature examined, 1000 K. Thermal annealing is performed experimentally at about 1100 K for 10 min [27]. Thus, the structural transformation from $V_O^{Al_2O_3}$ to $V_O^{SiO_2}$ via the diffusion of V_O occurs easily for such energy barriers. Moreover, even in the case of an activation barrier of 3.6 eV, since the occurrence rate

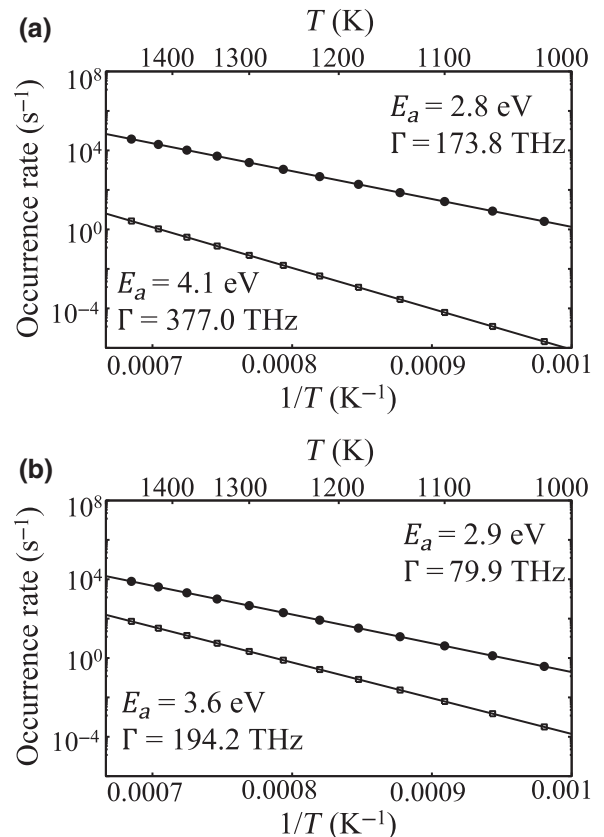


FIG. 11. Temperature dependence of the occurrence rate of the structural transformation from $V_O^{Al_2O_3}$ to $V_O^{SiO_2}$ via the diffusion of V_O in (a) $(Al_2O_3)_{0.70}(SiO_2)_{0.30}$ and (b) $(Al_2O_3)_{0.33}(SiO_2)_{0.67}$. E_a and Γ are the calculated energy-barrier height and the attempt frequency, respectively, for each reaction pathway.

is larger than $6.0 \times 10^{-3} s^{-1}$ at 1100 K [Fig. 11(b)], V_O diffusion takes place at least once during thermal annealing. When the energy barrier becomes larger, e.g., 4.1 eV, it is difficult to climb over the energy barrier under the experimental conditions. However, if the annealing temperature is raised to, for instance, 1250 K, the occurrence rate becomes $1.0 \times 10^{-2} s^{-1}$ even for a 4.1 eV barrier. An alternative way of making the reaction occur is, of course, to increase the annealing time. In any case, our calculations unequivocally make it clear that the structural transformation from $V_O^{Al_2O_3}$ to $V_O^{SiO_2}$ via V_O diffusion takes place with an energy barrier less than 3 eV and that the occurrence rate is high enough to make thermal annealing at 1100 K sufficient. This transformation is accompanied by the annihilation of the deep level induced by $V_O^{Al_2O_3}$, and conversion to electrically inactive $V_O^{SiO_2}$. It is thus predicted that postdeposition annealing will provide high-quality $(Al_2O_3)_{1-x}(SiO_2)_x$ mixed oxides, thus making such oxides a strong candidate for gate oxides with higher breakdown fields in GaN MOSFETs.

IV. CONCLUSION

We perform density-functional calculations that clarify the atomic and electronic structures of the oxygen vacancy V_O in amorphous $(\text{Al}_2\text{O}_3)_{1-x}(\text{SiO}_2)_x$ mixed oxides, which are a promising candidate for the gate insulator in GaN technology. The melt-quench scheme enables us to construct microscopic models for the amorphous structure with 11 different Si compositions x . We then examine all the possible oxygen vacancies, more than a hundred for each value of x , and determine the total-energy-minimized V_O structures. We find a clear tendency for V_O 's formed at oxygen sites surrounded by fewer Al atoms to have a lower formation energy. The formation-energy difference is substantial, up to 1.8 eV. More importantly, we find that a V_O surrounded by Si atoms alone induces no deep levels in the energy gap of GaN, whereas a V_O surrounded by some Al atoms induces a deep level. This theoretical finding strongly implies that the majority of V_O 's in amorphous $(\text{Al}_2\text{O}_3)_{1-x}(\text{SiO}_2)_x$ are electrically inactive and not very harmful to device operation. Further, we explore the possibilities for the structural transformation from the electrically active V_O to the electrically inactive V_O . We identify several distinct pathways for the diffusion of V_O that lead to such a structural transformation between active and inactive oxygen vacancies. The calculated energy barriers for the relevant reactions are less than 3 eV. Using transition-state theory, we calculate the occurrence rates for the possible structural transformations. The rates obtained are high enough to ensure that thermal annealing at typical temperatures and times causes conversion of the electrically active V_O to the electrically inactive V_O , providing a further advantage of $(\text{Al}_2\text{O}_3)_{1-x}(\text{SiO}_2)_x$ as a gate insulator for GaN MOSFETs over other oxides such as SiO_2 and Al_2O_3 .

ACKNOWLEDGMENTS

This work was supported by the Ministry of Education, Culture, Sports, Science, and Technology (MEXT), Japan, under the research projects “Social and Scientific Priority Issue (Creation of New Functional Devices and High-Performance Materials to Support Next-Generation Industries) To Be Tackled by Using Post-K Computer,” “Promoting Researches on the Supercomputer Fugaku,” and “Program for Research and Development of Next-Generation Semiconductors to Realize an Energy-Saving Society” under Contract No. JPJ005357, and also by Grants-in-aid under Contract No. 18H03873. Computations were performed with supercomputers at the Institute for Solid State Physics of The University of Tokyo and The Research Center for Computational Science of the National Institutes of Natural Sciences.

- [1] H. Okumura, Present status and future prospect of widegap semiconductor high-power devices, *Jpn. J. Appl. Phys.* **45**, 7565 (2006).
- [2] J. Biela, M. Schweizer, S. Stefan, and J. W. Kolar, SiC versus Si-evaluation of potentials for performance improvement of inverter and DC-DC converter systems by SiC power semiconductors, *IEEE Trans. Industr. Electron.* **58**, 2872 (2011).
- [3] N. Kaminski and O. Hilt, SiC and GaN devices—wide bandgap is not all the same, *IET Circ. Devices Syst.* **8**, 227 (2014).
- [4] M. Holtz, G. Hultsch, T. Scherg, and R. Rupp, Reliability considerations for recent Infineon SiC diode releases, *Microelectron. Reliab.* **47**, 1741 (2007).
- [5] V. V. Afanas'ev and A. Stesmans, Interfacial Defects in SiO_2 Revealed by Photon Simulated Tunneling of Electrons, *Phys. Rev. Lett.* **78**, 2437 (1997).
- [6] Y. Yano, F. Katafuchi, T. Kimoto, and H. Matsunami, Effects of wet oxidation/anneal on interface properties of thermally oxidized SiO_2/SiC MOS system and MOSFET's, *IEEE Trans. Electron Devices* **46**, 504 (1999).
- [7] G. Liu, B. R. Tuttle, and S. Dhar, Silicon carbide: A unique platform for metal-oxide-semiconductor physics, *Appl. Phys. Rev.* **2**, 021307 (2015).
- [8] I. Akasaki, Nobel lecture: Fascinated journeys into blue light, *Rev. Mod. Phys.* **87**, 1119 (2015).
- [9] H. Amano, Nobel lecture: Growth of GaN on sapphire via low-temperature deposited buffer layer and realization of *p*-type GaN by Mg doping followed by low-energy electron beam irradiation, *Rev. Mod. Phys.* **87**, 1133 (2015).
- [10] S. Nakamura, Nobel lecture: Background story of the inversion of efficient blue InGaN light emitting diodes, *Rev. Mod. Phys.* **87**, 1139 (2015).
- [11] B. J. Baliga, Semiconductors for high-voltage, vertical channel field-effect transistors, *J. Appl. Phys.* **53**, 1759 (1982).
- [12] B. J. Baliga, Gallium nitride devices for power electronic applications, *Semicond. Sci. Technol.* **28**, 074011 (2013).
- [13] R. Kajitani, K. Tanaka, M. Ogawa, H. Ishida, M. Ishida, and T. Ueda, Nobel high-current density GaN-based normally off transistor with tensile-strained quaternary InAlGaN barrier, *Jpn. J. Appl. Phys.* **54**, 04DF09 (2015).
- [14] H. Ishida, R. Kajitani, Y. Kinoshita, H. Umeda, S. Ujita, M. Ogawa, K. Tanaka, T. Morita, S. Tamura, M. Ishida, and T. Ueda, GaN-based semiconductor devices for future power switching systems, *IEDM Tech. Dig.*, 540 (2016).
- [15] J. Robertson and B. Falabretti, Band offsets of high K gate oxides on III-V semiconductors, *J. Appl. Phys.* **100**, 014111 (2006).
- [16] C. Bae and G. Lucovsky, Low-temperature preparation of GaN- SiO_2 interfaces with low defect density. I. Two-step remote plasma-assisted oxidation-deposition process, *J. Vac. Sci. Technol. A* **22**, 2402 (2004).
- [17] P. D. Ye, B. Yang, K. K. Ng, J. Bude, G. D. Wilk, S. Halder, and J. C. M. Hwang, GaN metal-oxide-semiconductor high-electron-mobility-transistor with atomic layer deposited Al_2O_3 as gate dielectric, *Appl. Phys. Lett.* **86**, 063501 (2005).
- [18] W. Huang, T. P. Chow, and T. Khan, Experimental demonstration of enhancement mode GaN MOSFETs, *Phys. Status Solidi A* **204**, 2064 (2007).

- [19] Y. C. Chang, W. H. Chang, H. C. Chiu, L. T. Tung, C. H. Lee, K. H. Shiu, M. Hong, J. Kwo, J. M. Hong, and C. C. Tsai, Inversion-channel GaN metal-oxide-semiconductor field-effect transistor with atomic-layer-deposited Al₂O₃as gate dielectric, *Appl. Phys. Lett.* **93**, 053504 (2008).
- [20] E. Ogawa and T. Hashizume, Variation of chemical and photoluminescence properties of Mg-doped GaN caused by high-temperature process, *Jpn. J. Appl. Phys.* **50**, 021002 (2011).
- [21] N. Taoka, T. Kubo, T. Yamada, T. Egawa, and M. Shimizu, Impacts of oxidants in atomic layer deposition method on Al₂O₃/GaN interface properties, *Jpn. J. Appl. Phys.* **57**, 01AD04 (2018).
- [22] N. X. Truyen, N. Taoka, A. Ohta, K. Makihara, H. Yamada, T. Takahashi, M. Ikeda, M. Shimizu, and S. Miyazaki, High thermal stability of abrupt SiO₂/GaN interface with low interface state density, *Jpn. J. Appl. Phys.* **57**, 04FG11 (2018).
- [23] T. Yamada, K. Watanabe, M. Nozaki, H. Yamada, T. Takahashi, M. Shimizu, A. Yoshigoe, T. Hosoi, and H. Watanabe, Control of Ga-oxide interface growth and Ga diffusion in SiO₂/GaN stacks for high-quality GaN-based metal-oxide-semiconductor devices with improved gate dielectric reliability, *Appl. Phys. Express* **11**, 015701 (2018).
- [24] K. Ito, D. Kikuta, T. Narita, K. Kataoka, N. Isomura, K. Kitazumi, and T. Mori, Band offset of Al_{1-x}Si_xO_y mixed oxide on GaN evaluated by hard X-ray photo-electron spectroscopy, *Jpn. J. Appl. Phys.* **56**, 04CG07 (2017).
- [25] C. Ostermaier, H.-C. Lee, S.-Y. Hyun, S.-I. Ahn, K.-W. Kim, H.-I. Cho, J.-B. Ha, and J.-H. Lee, Interface characterization of ALD deposited Al₂O₃ on GaN by CV method, *Phys. Status Solidi C* **5**, 1992 (2008).
- [26] Y. Hori, C. Mizue, and T. Hashizume, Process conditions for improvement of electrical properties of Al₂O₃/n-GaN structures prepared by atomic layer deposition, *Jpn. J. Appl. Phys.* **49**, 080201 (2010).
- [27] D. Kikuta, K. Itoh, T. Narita, and T. Mori, Al₂O₃/SiO₂ nanolaminate for a gate oxide in a GaN-based MOS device, *J. Vac. Sci. Technol. A* **35**, 01B122 (2017).
- [28] P. McMillan and B. Piriou, The structures and vibrational spectra of crystals and glasses in the silica-alumina system, *J. Non-Cryst. Solids* **53**, 279 (1982).
- [29] B. T. Poe, P. F. McMillan, B. Coté, D. Massiot, and J.-P. Coutures, SiO₂-Al₂O₃liquids in-situ study by high-temperature ²⁷Al NMR spectroscopy and molecular dynamics simulation, *J. Phys. Chem.* **96**, 8220 (1992).
- [30] J. A. Pask, Importance of starting materials on reactions and phase equilibria in the Al₂O₃-SiO₂system, *J. Eur. Ceram. Soc.* **16**, 101 (1996).
- [31] M. Okuno, N. Zotov, M. Schmücker, and H. Schneider, Structure of SiO₂-Al₂O₃glasses: Combined X-ray diffraction, IR and Raman studies, *J. Non-Cryst. Solids* **351**, 1032 (2005).
- [32] V. V. Hoang, Composition dependence of static and dynamic heterogeneities in simulated liquid aluminum silicate, *Phys. Rev. B* **75**, 174202 (2007).
- [33] Y. Yang, M. Takahashi, H. Abe, and Y. Kawazoe, Structural, electronic and optical properties of the Al₂O₃doped SiO₂: First principles calculations, *Mater. Trans.* **49**, 2474 (2008).
- [34] J. Ren, L. Zhang, and H. Eckert, Medium-range order in sol-gel prepared Al₂O₃-SiO₂glasses: New results from solid-state NMR, *J. Phys. Chem. C* **118**, 4906 (2014).
- [35] E. P. O'Reilly and J. Robertson, Theory of defects in vitreous silicon dioxide, *Phys. Rev. B* **27**, 3780 (1983).
- [36] M. Boero, A. Pasquarello, J. Sarnthein, and R. Car, Structure and Hyperfine Parameters of E' Centers in α -Quartz and in Vitreous SiO₂, *Phys. Rev. Lett.* **78**, 887 (1997).
- [37] A. Yokozawa, A. Oshiyama, Y. Miyamoto, and S. Kumashiro, Oxygen vacancy with large lattice distortion as an origin of leakage currents in SiO₂, *IEDM Tech. Dig.*, 703 (1997).
- [38] A. Oshiyama, Hole-injection-induced structural transformation of oxygen vacancy in α -quartz, *Jpn. J. Appl. Phys.* **37**, L232 (1998).
- [39] P. E. Blöchl, First-principles calculations of defects in oxygen-deficient silica exposed to hydrogen, *Phys. Rev. B* **62**, 6158 (2000).
- [40] M. Boero, A. Oshiyama, and P. L. Silvestrelli, E' Center in α Quartz in the Absence of Oxygen Vacancies: A First-Principles Molecular-Dynamics Study, *Phys. Rev. Lett.* **91**, 206401 (2003).
- [41] J. Carrasco, J. R. B. Gomes, and F. Illas, Theoretical study of bulk and surface oxygen and aluminum vacancies in α -Al₂O₃, *Phys. Rev. B* **69**, 064116 (2004).
- [42] N. D. M. Hine, K. Frensch, W. M. C. Foulkes, and M. W. Finnis, Supercell size scaling of density functional theory formation energies of charged defects, *Phys. Rev. B* **79**, 024112 (2009).
- [43] N. L. Anderson, R. P. Vedula, P. A. Schultz, R. M. Van Ginhoven, and A. Strachan, First-Principles Investigation of Low Energy E' Center Precursors in Amorphous Silica, *Phys. Rev. Lett.* **106**, 206402 (2011).
- [44] N. L. Anderson, R. P. Vedula, P. A. Schultz, R. M. Van Ginhoven, and A. Strachan, Defect level distributions and atomic relaxations induced by charge trapping in amorphous silica, *Appl. Phys. Lett.* **100**, 172908 (2012).
- [45] M. Choi, A. Janotti, and C. G. Van de Walle, Native point defects and dangling bonds in α -Al₂O₃, *J. Appl. Phys.* **113**, 044501 (2013).
- [46] M. Y. Yang, K. Kamiya, B. Magyari-Köpe, M. Niwa, Y. Nishi, and K. Shiraishi, Charge-dependent oxygen vacancy diffusion in Al₂O₃-based resistive-random-access-memories, *Appl. Phys. Lett.* **103**, 093504 (2013).
- [47] Z. Guo, F. Ambrosio, and A. Pasquarello, Oxygen defects in amorphous Al₂O₃: A hybrid functional study, *Appl. Phys. Lett.* **109**, 062903 (2016).
- [48] M. S. Munde, D. Z. Gao, and A. L. Shluger, Diffusion and aggregation of oxygen vacancies in amorphous silica, *J. Phys.: Condens. Matter* **29**, 245701 (2017).
- [49] E. Kojima, K. Chokawa, H. Shirakawa, M. Araida, T. Hosoi, H. Watanabe, and K. Shiraishi, Effect of incorporation of nitrogen atoms in Al₂O₃gate dielectric of wide-bandgap-semiconductor MOSFET on gate leakage current and negative fixed charge, *Appl. Phys. Express* **11**, 061501 (2018).
- [50] P. Hohenberg and W. Kohn, Inhomogeneous electron gas, *Phys. Rev. B* **136**, 864 (1964).

- [51] W. Kohn and L. J. Sham, Self-consistent equations including exchange and correlation effects, *Phys. Rev.* **140**, A1133 (1965).
- [52] G. Kresse and J. Furthmüller, Efficient iterative schemes for *ab initio* total-energy calculations using a plane-wave basis set, *Phys. Rev. B* **54**, 11169 (1996).
- [53] G. Kresse and D. Joubert, From ultrasoft pseudopotentials to the projector augmented-wave method, *Phys. Rev. B* **59**, 1758 (1999).
- [54] J. P. Perdew, K. Burke, and M. Ernzerhof, Generalized Gradient Approximation Made Simple, *Phys. Rev. Lett.* **77**, 3865 (1996).
- [55] J. Heyd, G. E. Scuseria, and M. Ernzerhof, Hybrid functionals based on a screened Coulomb potential, *J. Chem. Phys.* **118**, 8207 (2003).
- [56] P. E. Blöchl, Projector augmented-wave method, *Phys. Rev. B* **50**, 17953 (1994).
- [57] J. Lewis, D. Schwarzenbach, and H. D. Flack, Electric field gradients and charge density in corundum, α -Al₂O₃, *Acta Crystallogr. Sect. A* **38**, 733 (1982).
- [58] J. R. Gladden, J. H. So, J. D. Maynard, P. W. Saxe, and Y. Le Page, Reconciliation of *ab initio* theory and experimental elastic properties of Al₂O₃, *Appl. Phys. Lett.* **85**, 392 (2004).
- [59] L. Levien, C. T. Prewitt, and D. J. Weidner, Structure and elastic properties of quartz at pressure, *Am. Mineral.* **65**, 920 (1980).
- [60] P. Heyliger, H. Ledbetter, and S. Kim, Elastic constants of natural quartz, *J. Acoust. Soc. Am.* **114**, 644 (2003).
- [61] K. Momma and F. Izumi, VESTA 3 for three-dimensional visualization of crystal, volumetric and morphology data, *J. Appl. Crystallogr.* **44**, 1272 (2011).
- [62] R. Manaila, A. Dévényi, and E. Candet, Structural order in amorphous aluminas, *Thin Solid Films* **116**, 289 (1984).
- [63] S.-M. Lee, D. G. Cahill, and T. H. Allen, Thermal conductivity of sputtered oxide films, *Phys. Rev. B* **52**, 253 (1995).
- [64] K. Vollmayr, W. Kob, and K. Binder, Cooling-rate effects in amorphous silica: A computer-simulation study, *Phys. Rev. B* **54**, 15808 (1996).
- [65] R. M. Van Ginneken, H. Jónsson, and L. R. Corrales, Silica glass structure generation for *ab initio* calculations using small samples of amorphous silica, *Phys. Rev. B* **71**, 024208 (2005).
- [66] M. Kim, K. H. Khoo, and J. R. Chelikowsky, Simulating liquid and amorphous silicon dioxide using real-space pseudopotentials, *Phys. Rev. B* **86**, 054104 (2012).
- [67] J. M. D. Lane, Cooling rate and stress relaxation in silica melts and glasses via microsecond molecular dynamics, *Phys. Rev. E* **92**, 012320 (2015).
- [68] J. Bernholc, N. O. Lipari, and S. T. Pantelides, Self-Consistent Method for Point Defects in Semiconductors: Application to the Vacancy in Silicon, *Phys. Rev. Lett.* **41**, 895 (1978).
- [69] G. A. Baraff and M. Schlüter, Electronic Structure, Total Energies, and Abundances of the Elementary Point Defects in GaAs, *Phys. Rev. Lett.* **55**, 1327 (1985).
- [70] R. Car, P. J. Kelly, A. Oshiyama, and S. T. Pantelides, Microscopic Theory of Impurity-Defect Reactions and Impurity Diffusion in Silicon, *Phys. Rev. Lett.* **54**, 360 (1985).
- [71] M. Leslie and M. J. Gillan, The energy and elastic dipole tensor of defects in ionic crystals calculated by the supercell method, *J. Phys. C: Solid State Phys.* **18**, 973 (1985).
- [72] G. Makov and M. C. Payne, Periodic boundary conditions in *ab initio* calculations, *Phys. Rev. B* **51**, 4014 (1995).
- [73] C. Freysoldt, J. Neugebauer, and C. G. Van de Walle, Electrostatic interactions between charged defects in supercells, *Phys. Status Solidi B* **248**, 1067 (2011).
- [74] Y. Kumagai and F. Oba, Electrostatics-based finite size corrections for first-principles point defect calculations, *Phys. Rev. B* **89**, 195205 (2014).
- [75] G. A. Baraff, O. Kane, and M. Schlüter, Theory of the silicon vacancy: An Anderson negative-*U* system, *Phys. Rev. B* **21**, 5662 (1980).
- [76] R. Car, P. J. Kelly, A. Oshiyama, and S. T. Pantelides, Microscopic Theory of Atomic Diffusion Mechanisms in Silicon, *Phys. Rev. Lett.* **52**, 1814 (1984).
- [77] T. Kurita, K. Uchida, and A. Oshiyama, Atomic and electronic structures of α -Al₂O₃ surface, *Phys. Rev. B* **82**, 155319 (2010).
- [78] G. Mills, H. Jónsson, and G. K. Schenter, Reversible work transition state theory: Application to dissociative adsorption of hydrogen, *Surf. Sci.* **324**, 305 (1995).
- [79] G. Henkelman, B. P. Uberuaga, and H. Jónsson, A climbing image nudged elastic band method for finding saddle points and minimum energy paths, *J. Chem. Phys.* **113**, 9901 (2000).
- [80] D. Sheppard, P. Xiao, W. Chemelewski, D. D. Johnson, and G. Henkelman, A generalized solid-state nudged elastic band method, *J. Chem. Phys.* **136**, 074103 (2012).
- [81] J. D. Weeks, J. C. Tully, and L. C. Kimerling, Theory of recombination-enhanced defect reactions in semiconductors, *Phys. Rev. B* **12**, 3286 (1975).
- [82] R. Bader, *Atoms in Molecules: A Quantum Theory* (Oxford University Press, New York, 1990).
- [83] M. Yu and D. R. Trinkle, Accurate and efficient algorithm for Bader charge integration, *J. Chem. Phys.* **134**, 064111 (2011).
- [84] G. H. Vineyard, Frequency factors and isotope effects in solid state rate processes, *J. Phys. Chem. Solids* **3**, 121 (1957).